

STUDY OF THE BEHAVIOUR AND MECHANISM OF SLURRY العنوان:

> البخيتي، محمد احمد حمود علي المؤلف الرئيسي:

احمد، شيمي محمد، عمارة، كرم محمد موسى، بدران، فاروق محمد مؤلفين آخرين:

فرید(مشرف)

2005 التاريخ الميلادي:

اسيوط موقع:

1 - 212 الصفحات:

586715 رقم MD:

رسائل جامعية نوع المحتوى:

> **English** اللغة:

الدرجة العلمية: رسالة دكتوراه

جامعة اسيوط الجامعة:

كلية الهندسة الكلية:

الدولة:

Dissertations قواعد المعلومات:

الهندسة الميكانيكية، التآكل، السوائل، المواد الصلبة مواضيع:

https://search.mandumah.com/Record/586715 رابط:

© 2020 دار المنظومة. جميع الحقوق محفوظة.

ى عدد عبر مستوسد، جسيم العقوف المحقوف. هذه المادة متاحة بناء على الإتفاق الموقع مع أصحاب حقوق النشر، علما أن جميع حقوق النشر محفوظة. يمكنك تحميل أو طباعة هذه المادة للاستخدام الشخصي فقط، ويمنع النسخ أو التحويل أو النشر عبر أي وسيلة (مثل مواقع الانترنت أو البريد الالكتروني) دون تصريح خطي من أصحاب حقوق النشر أو دار المنظومة.



بسم الله الرحمن الرحيم

ملخم البحث حر اسة سلوك و آلية التآكل الناتج عن سريان سائل به عو الة صلية

في هذا البحث أجريت سلسله منهاجية من التجارب على التأكل الناتج عن سريان سائل به عوالق صلبة بغرض دراسة تأثير مختلف العوامل على سلوك وآليات التأكل لمواد طرية ومواد قصيفة هذه العوامل تشمل كل من زاوية التصادم وسرعة التصادم وتركيز الحبيبات الصلبة وخصائص تلك الحبيبات (الحجم والشكل والصلادة) وصلادة المادة المعرضة للتأكل وكذلك بنيتها الدقيقة. لاجراء هذه التجارب تم تصميم وتصنيع جهاز الاختبار ثم أجريت عليه سلسلة من التجارب لاختبار كفاءة وتكرارية ومعولية ذلك الجهاز باستخدام تقنية تعجيل ومشاهدة التأكل لطبقة طلاء مرشوشة على عينات من الصلب.

وقد أجريت التجارب المعملية على مادتين مختلفتين تستخدمان في صناعة أجزاء الماكينات وهما الحديد المنخفض الكربون (AISI 1017 steel) وحديد الزهر الابيض عالي الكروم وباستخدام ثلاثة أنواع مختلفة من الحبيبات الصلبة الصادمة وهي الرمل وكربيد السليكون والألومينا والسائل الحامل لهذة الحبيبات هو الماء. تم استخدام المجهر الالكتروني الماسح والمجهر الضوئي ومحلل الصورة وجهاز قياس الصلادة وميزان الكتروني حساس (حساسيته 0.1 مجم) في تحديد آليات التآكل وسلوكه.

بالفحص الدقيق والتحليل للصور المجهرية لأسطح العينات التى حدث بها تأكل أتضح أن آليات التأكل للحديد المنخفض الكربون هي آلية الحرث وآلية القطع الدقيق وآلية التّلمة بشفاه مبثوقة وكذلك آلية الكلال. بينما في حالة حديد الزهر عالي الكروم فإن آلية التآكل تعتمد على تركيب البنية الدقيقة، ففي حالة الأرضية الطرية تكون آليات التآكل مشابهة تماما الما هو عليه في الحديد المنخفض الكربون بينما للجزء الآخر من البنية وهي الكاربيدات الصلبة فإن آلية التآكل هي التشرخ والتكسر الإجمالي، وقد لوحظ اعتماد آليات التآكل على ظروف الاختبار فعند دراسة تأثير أحد العوامل على آليات التآكل وجد أن آلية واحدة أو أكثر تلعب الدور الرئيسي في ازالة المادة من سطح التآكل بينما الآليات الأخرى

تكون ذات تأثير مهمل. وقد وجد أن تحديد آليات التآكل ساعد كثيرا في تفسير تأثير العوامل المختلفة على معدل التآكل المستقر.

تأثير زاوية التصادم على آليات التآكل للحديد منخفض الكربون أمكن تقسيمه إلى ثلاث مناطق هي منطقة الزوايا الصغيرة والتي تكون فيها الزاوية أقل من 20° ومنطقة الزوايا المتوسطة والمحصورة ما بين 20° و و 70° ومنطقة الزوايا الكبيرة وتكون لزوايا أكبر من 70°. هذا التقسيم أو المناطق الثلاث متعلق بالمركبة المماسية والمركبة العمودية لقوة التصادم. ففي المنطقة الأولى كانت أليات التآكل المسيطرة هي آلية الحرث الضحل وتدحرج الحبيبات على السطح والتي نتج عنها معدلات تآكل صغيرة. في المنطقة الثانية لعب فيها آلية القطع الدقيق وآلية الحرث العميق الدور الرئيسي مما أدي إلى أعلى معدل تآكل أما في المنطقة الثالثة تكون فيها آلية الثامات المحاطة بشفاه مما أدى إلى إنخفاض معدل التآكل.

بالنسبة لتأثير زاوية التصادم على الحديد الزهر عالى الكروم فامكن تقسيمه الى منطقتين المنطقة الأولى وكانت فيها زاوية التصادم أقل من °45 والثانية لزوايا تصادم أكبر من ذلك. ففي المنطقة الأولى كانت آلية التآكل هي التشكيل اللذن للأرضية الطرية والتي أدت إلى معدل تآكل منخفض أما في المنطقة الثانية فقد سادها كل من آليتي التشكيل اللذن للأرضية الطرية وتكسر وتشرخ للكاربيدات في آن واحد مما أدى الى تآكل أعلى ما يمكن عند زاوية تصادم °90 .

ولفحص تأثير خصائص الحبيبات الصلبة أي نوعها وحجمها وشكلها وصلادتها على آليات التأكل ودورها في تطور التآكل فقد تم توصيف الأنواع الثلاثة من الحبيبات الصلبة (الرمل، كربيد السليكون، والألومينا) بمعرفة معامل "تحديد الشكل" وهو العرض إلى الطول ومعامل الاستدارة ويساوي مربع محيط الحبيبة الى مساحتها. وبناءاً على ذلك وجد أن الانتظام والاستدارة في الشكل لحبيبات الرمل والألومينا تزداد مع زيادة حجمهما بينما تتناقص لحبيبات كاربيد السيليكون. فبالنسبة لتأثير حجم الحبيبات الصلبة وجد أن الأحجام الصغيرة للأنواع الثلاثة من الحبيبات ينتج عنها تأثير واحد وهو تكون تلمات مصحوبة ببثق للمادة في كل من الحديد المنخفض الكربون والأرضية الطرية لحديد الزهر عالي الكروم. أما بالنسبة لتأثير الأحجام الكبيرة لحبيبات الرمل وكاربيد السليكون على الحديد المنخفض الكربون وعند زاوية تصادم "30 لوحظ أن آليتي الحرث والقطع الدقيق هما المسيطرتان ويزداد دور آلية التآكل بالقطع الدقيق بزيادة درجة تزوي الحبيبات الصلبة وعدم انتظام شكلها كما هو الحال في حبيبات كاربيد السليكون. كما أن التزو وحدية حواف حبيبات كاربيد السليكون تنتج مسارات تآكل خشنة ومشرشرة مقارنة بمسارات التآكل المستوية والناعمة التي تنتج عن حبيبات تتحديدات

الرمل ذات الشكل المنتظم والمدَّور لنفس الحجم. كما أنه شوهد أن الشفاه للثَّلمات والمادة المزاحة أمام وعلى جوانب المسار في حالة الحرث تنفصل من سطح التآكل بواسطة آلية الكلال.

أمّا عن تاثير أحجام الحبيبات الكبيرة على حديد الزهر عالي الكروم وعند زاوية تصادم عمودية (90°) حيث يكون التآكل أكبر ما يمكن أتضح أن آليتي التكسر والتشرخ يحدثان لطور الكاربيدات الصلبة بالإضافة إلى آلية الثّلمات ذات الشفاه للأرضية الطرية للمعدن معتمدا على شكل الحبيبة. فحبيبات كاربيد السليكون الغير منتظمة الشكل وذات الحواف الحادة ينتج عنها تكسر إجمالي للكاربيدات الصلبة مع تشرّخ جانبي للكاربيدات أيضا بالإضافة إلى التشوه اللدن للأرضية الطرية مما يؤدي الى تآكل عال في حين أن الحجم المماثل له من حبيبات السليكا والتي لها شكل منتظم ومستدير تعطي تآكلا أقل. واظهرت النتائج أيضا أن صلادة الحبيبات المسببة للتآكل مقارنة بصلادة المعدن لها تأثير جلي على آلية التآكل.

بالنسبة لسرعة الحبيبات الصادمة ودورها في تطور عملية التآكل أتضح أنه مقترن بآليات التآكل والتي تعتمد بدورها على طاقة الحركة لتلك الحبيبات. فللحديد منخفض الكربون وعند زاوية تصادم °30 وجد أن آلية التآكل تتغير من مجرد تكون تلمات ذات شفاه عند سرعة تصادم صغيرة (5 m/s) إلى حرث ذو مسار قصير عند السرعة المتوسطة (m/s) وحرث ذو مسار طويل السرعة العالية (m/s). أما لحديد الزهر عالي الكروم وزاوية تصادم °90 فاعتماد آلية التآكل على السرعة يكون مرتبط أيضا ببنية المادة الدقيق فلسرعة تصادم صغيرة (m/s) تحدث تلمات فقط في الأرضية الطرية ولسرعة تصادم متوسطة (m/s) تزداد التلمات في الأرضية الطرية بالاضافة إلى الكسر في الكربيدات. بينما لسرعة تصادم أعلى (m/s) يحدث تكسر وتشرخ أكثر الكاربيدات بالاضافة الى النامات في الأرضية الطرية.

وتناول البحث أيضا تاثير تركيز الحبيبات الصلبة في السائل على كل من الحديد منخفض الكربون وحديد الزهر عالي الكروم وأتضح أن الفقد في وزن العينة نتيجة التآكل يزداد مع زيادة نسبة التركيز بينما معدل التآكل (الفقد في الوزن/وزن الحبيبات الصادمة) يزداد عند نسب التركيز الصغيرة ثم يتناقص بعد ذلك مع زيادة نسبة التركيز. وبفحص الصور المجهرية الدقيقة الأسطح العينات المتعرضة للتآكل عند نسبتي تركيز هما %. wt. و % وزن الحبيبات الى وزن السائل) أتضح أن آلية التآكل لا تعتمد على نسبة التركيز بينما شدية التآكل تزداد مع زيادة نسبة التركيز وذلك راجع إلى زيادة عدد الحبيبات الصادمة مما ينتج عنه زيادة في حجم أثر التآكل.

Abstract

In the present work a series of systematic slurry erosion tests were carried out to investigate the effect of different parameters on slurry erosion mechanisms and behaviour for ductile and brittle materials. These parameters include impingement angle, impact velocity, particle concentration, erodent particle characteristics, namely size, shape and hardness as well as target material hardness and microstructure. An apparatus for carrying out slurry erosion experiments was designed and manufactured. A series of accelerated erosion tests using a paint erosion indication technique has been carried out to calibrate and examine the reproducibility, capability and performance of the designed test rig.

The slurry erosion tests were carried out using the designed test rig on two different machinery materials, namely AISI 1017 steel and high-chromium white cast iron; and using three different types of erodent particles, namely silica sand, silicon carbide and alumina. The scanning electron microscopy, computer aided-image analysis technique, optical microscopy and gravimetric and microhardness measurements were utilized to identify the slurry erosion process.

Observations and analysis of the scanning electron microphotographs of specimen surfaces impacted for a short time at different slurry erosion conditions revealed that for 1017 steel the slurry erosion mechanisms are: ploughing, microcutting, indentation with extruded lips and fatigue wear. While, for high-Cr white cast iron the slurry erosion mechanisms are: cracking and gross fracture of the carbide phases as well as ploughing, microcutting and indentation with extruded lips for the ductile matrix. It was found that, in each particular case (test conditions) one or more of these mechanisms play the main role in the metal removal process, while others have a minor effect or not at all. Determination of the erosion mechanisms

helped greatly in the interpretation of the effect of the different parameters on the erosion rate in steady-state tests.

Test results showed that, the effect of impingement angle on erosion mechanisms of 1017 steel has three regions. These regions are: region of small impingement angles less than 20°, region of intermediate impingement angles between 20° and 70° and finally region of high impingement angles greater than 70°. These three regions are related to the tangential and normal components of the impacting force. The first region was characterized by shallow long scratches and limited chip formations resulting in small erosion rate. In the second region the formed wear tracks have deep and wide size and large chips were formed in front of the wear tracks, which explain the high erosion rate at intermediate impingement angles (maximum occurred at 45°). The third region was distinguished with relatively deep and elongated indentations with extruded material and small erosion rate. Consequently, it can be said that shallow ploughing and particle rolling were the dominant erosion mechanisms in the first region, microcutting and deep ploughing in the second region while indentations and material extrusion prevailed in the third region. For high-Cr white cast iron the test results showed that, the erosion mechanisms involved both plastic deformation of the ductile matrix and brittle fracture of the carbides. At low impingement angles (up to 45°) observations of microphotographs of the impacted surfaces revealed that, plastic deformation of the ductile matrix was the dominant erosion mechanism and the carbides fracture was negligible which lead to small erosion rate. Whereas, at high impingement angles (greater than 45°) gross fracture and cracking of the carbides in addition to indentation with extruded lips of the ductile matrix were the main erosion mechanisms.

The erodent particles, namely silica sand, silicon carbide and alumina were characterized in terms of their area (A), average diameter (d_{ave}), perimeter (P), length (L) and width (W). The aspect ratio (W/L) and the roundness factor ($P^2/4\pi A$) were used as the indicators of particle shape. It was found that the regularity and circularity

in shape of silica sand and alumina particles increased with the increase of particle sizes, while decreased for silicon carbide particles. Test results revealed that, with fine erodent particles plastic indentation accompanied by extruded material was the dominant erosion mechanism for 1017 steel and high-Cr white cast iron irrespective of the impingement angle and erodent type or shape. For 1017 steel and at impingement angle of 30°, results showed that ploughing and microcutting were the main erosion mechanisms when the target surface is impacted by coarse SiC and SiO₂ particles. The role of microcutting in the metal removal process increased with the increase of particle angularity and sharpness as in the case of silicon carbide particles. As well as the angularity and sharpness of silicon carbide particles yielded serrated tracks rather than smooth tracks obtained with regular and rounded silica sand particles for the same size. It was also shown that the lips and chips formed due to indentation and ploughing mechanisms were finally detached from the target surface by fatigue. It was also observed that microcracks initiated at many locations on the eroded area such as, chips and lips which were subjected to severe plastic deformation, serrations of ploughing tracks and traces of polishing lines. For high-Cr white cast iron and at normal incidence, test results showed that with impacting by coarse particles, fracture and cracking of the carbides in addition to plastic indentation with lips of the ductile matrix were the main erosion mechanisms depending on the particle shape. The angularity and sharpness of silicon carbide particles yielded severe erosion damage included gross fracture associated with formation of many lateral cracks of the carbides rather than mild erosion damage obtained with regular and rounded silica sand particles for a comparable size. The results also showed that the hardness of erodent particles has a pronounced effect on the material removal mechanism.

Test results showed that the role of the impact velocity in developing erosion damage is related to the variation of the erosion mechanisms which depend upon the kinetic energy of the impacting particles. At low impact velocity (5 m/s) and at impingement angle of 30°, microscopic observations of damaged surfaces of 1017 steel revealed that, indentation with extruded lips was the dominant erosion

mechanism. Whereas, at high impact velocity ploughing was the main erosion mechanism. The length of the wear tracks developed by ploughing mechanism depends upon the impact velocity. For high-Cr white cast iron and at normal incidence, test results showed that the erosion mechanism of indentation with extruded lips of the ductile matrix prevailed at low impact velocity (5 m/s). Whereas, at intermediate impact velocity (10 m/s) plastic indentation of the ductile matrix in addition to some fracture of the carbides were the dominant erosion mechanisms. For high impact velocity (15 m/s) fracture and cracking of the carbides besides to indentation of the ductile matrix were the dominant erosion mechanisms.

Test results showed that the weight loss from the surface of the test specimens increases with the increase of solid particle concentration. But the erosion rate (expressed in terms of mass loss per mass of crodent particles) increases at low particle concentration up to 1 wt.%. Then it decreases rapidly attaining nearly steady state behaviour. Observations of scanning electron microphotographs revealed that the erosion mechanisms at particle concentration of 1 wt.% and 3 wt.% are the same. It was also observed that the intensity of erosion damage at particle concentration of 3 wt.% is higher than that for particle concentration of 1 wt.%. This was attributed to repeated multiple impacts which occur at higher particle concentration resulting in large sizes of wear scar.



STUDY OF THE BEHAVIOUR AND MECHANISM OF SLURRY العنوان:

> البخيتي، محمد احمد حمود على المؤلف الرئيسي:

احمد، شيمي محمد، عمارة، كرم محمد موسى، بدران، فاروق محمد مؤلفين آخرين:

فرید(مشرف)

2005 التاريخ الميلادي:

اسيوط موقع:

1 - 212 الصفحات:

586715 رقم MD:

رسائل جامعية نوع المحتوى:

> **English** اللغة:

رسالة دكتوراه الدرجة العلمية:

جامعة اسيوط الحامعة:

كلية الهندسة الكلىة:

> الدولة: مصر

Dissertations قواعد المعلومات:

الهندسة الميكانيكية، التآكل، السوائل، المواد الصلبة مواضيع:

https://search.mandumah.com/Record/586715 رابط:

© 2020 دار المنظومة. جميع الحقوق محفوظة. هذه المادة متاحة بناء على الإتفاق الموقع مع أصحاب حقوق النشر، علما أن جميع حقوق النشر محفوظة. يمكنك تحميل أو طباعة هذه المادة للاستخدام هذه المنخصي فقط، ويمنع النسخ أو التحويل أو النشر عبر أي وسيلة (مثل مواقع الانترنت أو البريد الالكتروني) دون تصريح خطي من أصحاب حقوق النشر أو المستخصي فقط، ويمنع النسخ أو التحويل أو النشر عبر أي وسيلة (مثل مواقع الانترنت أو البريد الالكتروني) دون تصريح خطي من أصحاب حقوق النشر أو دار المنظومة.



Table of Contents

Chapter		page
I.	Introduction and Literature Review	1
	1-1 Introduction	1
	1-2 Literature Review	4
	1-3 Impingement Angle	4
	1-4 Particle Velocity	7
	1-5 Particle Concentration	10
	1-6 Particle Characterization	13
	1-6-1 Particle size	13
	1-6-2 Particle shape	14
	1-6-3 Particle hardness	17
	1-6-4 Particle degradation	18
	1-7 Target Material Properties	19
	1-8 Test Methods	21
	1-8-1 Pipelines	21
	1-8-2 Laboratory test rigs	22
	 i Jet impingement tester ii A centrifugal erosion test fixture iii Flow-through slurry wear test equipment iv Slurry pot testers 	22 22 22 24
	1-9 Scope of the Present Work	27
I	II. Experimental Work	28
	2-1 Introduction	28
	2-2 Slurry Erosion Test Rig	. 29
	2-2-1 Calibration	. 33
	2-2-2 Determination of test parameters	35

velocity	. 35 . 37
2and Capability of the Designed Apparatus	
Per mance of the tester with four rotating arms	. 37
2-3 Per aducibility of the tester	. 38
oducibility of the tester	40
fiability of the tester	42
1- Effect of exposure time 2- Effect of impingement angle 3- Effect of impact velocity 4- Effect of particle concentration	. 42 45 45 48
arget Materials	50
2-4-1 AISI 1017 Steel	50
2-4-2 High-chromium white cast iron	
2-5 Erodent Particles	52
2-6 Measuring Devices	57
	58
1- Topographic features of eroded surfaces	58 58
3- Erodent particle characterization	58
4- Surface roughness measurement	58
5- Microhardness measurement	59
2-7 Experimental Procedure	59
III. Effect of Impingement Angle on Slurry Erosion Behaviour and	
Mechanisms	61
3-1 Introduction	61
3-2 Effect of Impingement Angle on Erosion Beahviour and Mechanisms of 1017 Steel	61
3-2-1 Erosion rate	61
3-2-2 Configuration of eroded surfaces	62
3-2-3 Microscopy observations of impacted surfaces	64 73
3-3 Effect of Impingement Angle on Erosion Behaviour and Mechanisms of High-Cr White Cast Iron	78
3-3-1 Erosion rate	80
3-3-2 Microscopy observations and erosion mechanisms	80

3-4 Erosion Behaviour and Mechanisms of 1017 Steel and High-Cr White Cast Iron with Impingement Angles	87
IV. Effect of Particle Characteristics on Slurry Erosion Behaviour and Mechanisms	91
4-1 Erodent Particle Characterization	91
4-2 Effect of Particle Characteristics on Erosion Rate	101
4-2-1 Effect of particle size	101 105 106
4-3 Microscopy Observations and Erosion Mechanisms of 1017 Steel	108
4-3-1 Effect of particle size	108 112 114 114
4-4 Microscopy Observations and Erosion Mechanisms of High-Cr White Cast Iron	121
4-4-1 Effect of particle size	121 130 134
V. Effect of Impact Velocity and Particle Concentration on Slurry Erosion Behaviour and Mechanisms	136
5-1 Effect of Impact Velocity on Erosion Rate	136
5-2 Effect of Particle Concentration on Erosion Rate	138
5-3 Microscopy Observations and Erosion Mechanisms of 1017 Steel	141
5-3-1 Effect of impact velocity	141 149
5-4 Microscopy Observations and Erosion Mechanisms of High-Cr White Cast Iron	149
5-4-1 Effect of impact velocity	149 159
VI. Conclusions	164

References]	168
Appendices		
A. Analysis of the rotating arms dynamics of the designed apparatus	•••	179
B. Solidification sequences and microstructure of high-Cr white cast iron		
alloy	• •	184

List of Tables

Table		page
1-1	Parameters influencing slurry erosion	2
1-2	Experimental values of the velocity exponent n for slurry erosion reported in the literature	9
2-1	Results of reproducibility tests	42
2-2	Chemical composition of 1017 steel	52
2-3	Mechanical properties of 1017 steel	52
2-4	Chemical composition of high-Cr white cast iron alloy	55
2-5	Bulk hardness and microhardness of high-Cr white cast iron alloy	55
2-6	Size ranges and suppliers of particles	57
2-7	Values of the studied slurry erosion parameters and test conditions	60
4-1	Statistical values of particle parameters (size and shape) as obtained by image analysis processing of SiO ₂ particles	97
4-2	Statistical values of particle parameters (size and shape) as obtained by image analysis processing of SiC particles	97
4-3	Statistical values of particle parameters (size and shape) as obtained by image analysis processing of Al ₂ O ₃ particles	98
A-1	Calculated values of the specimen surface length which is exposed to the slurry stream at: $v = 10$ m/s, $v_2 = 9.89$ m/s, $N = 12.7$ Hz and $\theta' = 9.2^{\circ}$, using four rotating arms	182
A-2	Calculated values of the specimen surface length which is exposed to the slurry stream at: $v = 15$ m/s, $v_2 = 14.96$ m/s, $N = 19.2$ Hz and $\theta' = 6.3^{\circ}$, using four rotating arms	182

A-3	Calculated values of the specimen surface length which is exposed to the slurry stream at: $v = 15$ m/s, $v_2 = 14.96$ m/s, $N = 19.2$ Hz and $\theta' = 6.3^{\circ}$, using two rotating arms	182
A-4	Calculated values of the specimen surface length which is exposed to the slurry stream at: $v = 20$ m/s, $v_2 = 19.95$ m/s, $N = 25.6$ Hz and $\theta' = 4.6^{\circ}$, using two rotating arms	183

List of Figures

Figure		page
1-1a	Erosion of needle in needle and seat choke [12]	3
1-1b	A Pelton turbine runner destroyed by advanced wall erosion [13]	3
1-1c	Surface erosion of the inside of a Francis turbine [13]	3
1-1d	Eroded stainless steel needle of a 2-nozzle Pelton turbine [13]	3
1-1e	Pump impeller failure due to erosion [14]	3
1-2	Erosion rate as a function of impact angle for Aluminum, Copper, Mild steel and Alumina eroded by silica sand (600-1000 μ m), slurry at $\nu = 5.3$ m/s and C = 17 wt. % [20]	6
1-3	 (a) Dependence of erosion rate for Al₂O₃ on impact angle. (b) Dependence of erosion rate for zirconia, silaon and SiC on impact angle [21] 	6
1-4	Erosion vs. slurry velocity for hot-rolled 1018 steel in 30 wt.% coal-kerosene slurry at 95°C at various impingement angles [40]	8
1-5	Velocity-wear relationship: •, Aluminum; O, Cast iron; +, Ceramic Steel [41]	8
1-6	Relationship between wear rate and jet velocity [6]	8
1-7	Effect of velocity on the erosion rate of iron for a range of erodent sizes: (a) alumina and (b) silicon carbide [42]	11
1-8	Relationship between wear rate and silica sand concentration [6]	12
1-9	Variation of erosion rate as a function of cumulative weight of the erodent under oblique impact angle for Ni in A2-treated condition [47]	12
1-10	Relationship between wear rate and particle size [6]	15

1-11	Definition of particle size by means of three mutually perpendicular dimensions [60]	15
1-12	Schematic diagram of the pilot plant [93]	23
1-13	Schematic diagram of slurry jet erosion rig [41]	23
1-14	Schematic diagram of a centrifugal slurry erosion test fixture [95]	25
1-15	Schematic diagram of flow-through slurry wear test apparatus [95]	25
1-16	Schematic diagram of the slurry erosion pot tester [50]	26
2-1	Schematic diagram of the designed slurry erosion apparatus	30
2-2a	Photograph of the slurry erosion test rig, "General view"	31
2-2b,c	Photograph of the designed slurry erosion test rig: (b) Vacuum test chamber and (c) Rotating test specimens exposed to falling slurry stream	32
2-3	Schematic diagram of the specimen holder and the impingement angle indicator	34
2-4	Calibration curve for the speed controller unit	34
2-5	Measured rate of slurry flow and solid particle concentration in slurry: (a) $C = 2$ wt. % and (b) $C = 10$ wt. %, erodent (250-355 $\mu m SiO_2$)	36
2-6	Schematic diagram of impact velocity and impingement angle	39
2-7	Photographs of the eroded paint surfaces using four rotating arms at different test durations and test conditions: $v = 15$ m/s, $C = 1$ wt. % and $d = 302$ μ m; (a) $\theta = 30^{\circ}$, (b) $\theta = 45^{\circ}$, (c) $\theta = 60^{\circ}$ and (d) $\theta = 90^{\circ}$	39
2-8	Schematic diagram of (a) four rotating arms, (b) resultant angle of impact and (c) dynamic location of specimens with respect to the falling slurry stream	41

2-9	Photographs of the eroded paint surfaces using two rotating arms at test conditions: $v = 15$ m/s, $C = 1$ wt. %, $d = 302$ μ m and $t = 4$ min	41
2-10	Photographs of the eroded paint surfaces at different test durations and test conditions as: $v = 15$ m/s, $d = 302$ μ m, and $C = 1$ wt.%	44
2-11	Erosion rate of paint material as a function of test duration for different impingement angles at: $v = 15$ m/s, $d = 302$ µm and $C = 1$ wt. %	44
2-12	Photographs of the eroded paint surfaces at different impingement angles and test conditions as: $v = 15$ m/s, $d = 302$ μ m, $C = 1$ wt.% and $t = 4$ min.	46
2-13	Relationship between erosion rate of paint material and impingement angle at: $v = 15$ m/s, $d = 302$ μ m, $C = 1$ wt. %, and $t = 4$ min	46
2-14	Photographs of the eroded paint surfaces at different impact velocities and test conditions as: $d = 302 \mu m$, $C = 1 \text{ wt.}\%$ and $t = 4 \text{ min.}$	47
2-15	Relationship between erosion rate of paint material and impact velocity for different impingement angles at: $d = 302 \mu m$, $C = 1 wt$. %, and $t = 4 min$.	47
2-16	Variation of weight loss of the paint material versus particle concentration at different impingement angles and at: $v = 15$ m/s, $d = 302 \mu m$ and $t = 2$ min.	49
2-17	Relationship between weight loss of paint material and particle concentration for different impingement angles at: $v = 15$ m/s, $d = 302$ μm and $t = 2$ min.	49
2-18	Dimensions of (a) Slurry erosion test specimen and (b) Holder of the test specimen	51
2-19	Optical (a) and SEM (b) photographs of 1017 steel microstructure	54
2 - 20a,b	Optical photographs of High-Cr white cast iron microstructure	54
2-21a,b	SEM photographs of high-Cr white cast iron microstructure	54
2-22	Fe-Cr-C ternary phase diagram: (a) liquidus surface projection of the system and (b) isothermal section at 700°C	56

3-1	Cumulative Mass loss of 1017 steel as a function of test duration for different impingement angles	63
3-2	Relationship between erosion rate of 1017 steel and impingement angle for different test durations	63
3-3	Photographs of 1017 steel eroded surfaces at different values of impingement angles and at test time of (a) 10 min. and (b) 60 min	65
3-4	Relationship between the micro-hardness of 1017 steel eroded surfaces and impingement angle after test time of 60 min.	65
3-5	Scanning electron microphotographs of 1017 steel impacted surfaces at various impingement angles: (a) 15°, (b) 30°, (c) 45°, (d) 60° and (e) 90°	67
3-6	Scanning electron microphotographs of 1017 steel impacted surfaces at various impingement angles: (a) 15°, (b) 30°, (c) 45°, (d) 60° and (e) 90°. "Magnified views of selected areas from Fig. (3-5)"	70
3-7	Scanning electron microphotographs of 1017 steel impacted surfaces at various impingement angles: (a) 15°, (b) 30°, (c) 45°, (d) 60°, (e) 75° and (f) 90°.	74
3-8	Scanning electron microphotographs of 1017 steel impacted surfaces at high impingement angles: (a) 75° and (b) 90°. "Indented pits and extruded lips	79
3-9	Cumulative Mass loss of high-Cr white cast iron as a function of test duration for different impingement angles	81
3-10	Relationship between erosion rate of high-Cr white cast iron and impingement angle for different test durations	81
3-11	Scanning electron microphotographs of high-Cr white cast iron impacted surfaces at different impingement angles: (a) 30°, (b) 45°, (c) 60° and (d) 90°	82
3-12	Scanning electron microphotographs of high-Cr white cast iron impacted surfaces at different impingement angles: (a) 30°, (b) 45°, (c) 60° and (d) 90°.	85

3-13	function of erosion rate and erosion mechanisms of 1017 steel as a function of impingement angle at impact velocity of 15 m/s	89
3-14	Variation of erosion rate and erosion mechanisms of high-Cr white cast iron as a function of impingement angle at impact velocity of 15 m/s	90
4-1	Scanning electron microphotographs of silica sand particles	93
4-2	Scanning electron microphotographs of silicon carbide particles	94
4-3	Scanning electron microphotographs of alumina particles	96
4-4	Relationship between the aspect ratio and the measured average size for SiO ₂ , SiC and Al ₂ O ₃ particles	99
4-5	Relationship between the roundness factor (perimeter) ² / 4π Area and the measured average size for SiO ₂ , SiC and Al ₂ O ₃ particles	99
4-6	Percent cumulative frequency distribution curve of aspect ratios of SiO ₂ particles	100
4-7	Percent cumulative frequency distribution curve of aspect ratios of SiC particles	100
4-8	Percent cumulative frequency distribution curve of aspect ratios of Al ₂ O ₃ particles	100
4-9	Percent cumulative frequency distribution curve of $(perimeter)^2/4\pi Area$ ratios of SiO ₂ particles	102
4-10	Percent cumulative frequency distribution curve of (perimeter) $^2/4\pi$ Area ratios of SiC particles	102
4-11	Percent cumulative frequency distribution curve of (perimeter) $^2/4\pi$ Area ratios of Al ₂ O ₃ particles	102
4-12	Variation of erosion rate of 1017 steel as a function of particle sizes for different erodents, $\theta = 30^{\circ}$	103
4-13	Variation of erosion rate of high-Cr white cast iron as a function of particle sizes for different erodents, $\theta = 30^{\circ}$	103

4-14	Variation of erosion rate of 1017 steel as a function of particle sizes for different erodents, $\theta = 90^{\circ}$	104
4-15	Variation of erosion rate of high-Cr white cast iron as a function of particle sizes for different erodents, $\theta = 90^{\circ}$	104
4-16	Relationship between the erosion rate of 1017 steel and the relative hardness of the erodent particles and target material at $v = 15$ m/s, $d = (125-180 \mu m)$, $\theta = 30^{\circ}$ and $C = 1$ wt. %	107
4-17	Relationship between the erosion rate of high-Cr white cast iron and the relative hardness of the erodent particles and target material at $v=15$ m/s, $d=(125-180 \mu m)$, $\theta=30^{\circ}$ and $C=1$ wt. %	107
4-18	Scanning electron microphotographs of 1017 steel impacted surfaces at $\theta=30^{\circ}$ by different particles having different sizes: (a) SiO ₂ , $d=500-710$ µm; (b) SiO ₂ , $d=90-125$ µm; (c) SiC, $d=24$ grit; (d) SiC, $d=220$ grit and (e) Al ₂ O ₃ , $d=90-125$ µm	109
4-19	Calculated trajectories of sand particles of different diameters in a water jet 20 mm wide and velocity 8 m/s directed at flat plate [121]	111
4-20	Scanning electron microphotographs of 1017 steel impacted surfaces at $\theta = 30^{\circ}$ by coarse particles of (a) SiO ₂ and (b) SiC. "Magnified views of central areas selected from Fig. (4-18)"	113
4-21	Scanning electron microphotographs illustrating typical examples of (a) rounded SiO ₂ and (b) angular SiC particles	115
4-22	Scanning electron microphotographs of 1017 steel impacted surfaces at $\theta = 30^{\circ}$ by coarse particles of (a) SiO ₂ and (b) SiC. "Letter R denotes formation of microcrack on some traces of polishing lines	116
4-23	Scanning electron microphotographs of 1017 steel impacted surfaces at $\theta = 30^{\circ}$ by coarse SiC particles. The letter C indicates the formation of microcrack on the impacted surface	118
4-24	Scanning electron microphotographs of 1017 steel impacted surfaces at $\theta = 30^{\circ}$ by fine particles of (a) SiO ₂ , (b) SiC and (c) Al ₂ O ₃	118

4-25	Scanning electron microphotographs of 1017 steel impacted surfaces at $\theta = 30^{\circ}$ by fine particles of (a) SiO ₂ and (b) SiC. Directionality is clear in the surface features	120
4-26	Schematic for particle impacting on a target surface: (a) angular particle with positive rake angle, α , (b) rounded particle with negative rake angle and (c) angular particle with negative rake angle	122
4-27	Scanning electron microphotographs of 1017 steel impacted surfaces at $\theta = 30^{\circ}$ by coarse particles of (a) SiO ₂ and (b) SiC	122
4-28	Scanning electron microphotographs of high-Cr white cast iron impacted surfaces at $\theta = 90^{\circ}$ by different particles having different sizes: (a) SiO ₂ , d = 500-710 μ m; (b) SiO ₂ , d = 90-125 μ m; (c) SiC, d = 24grit; (d) SiC, d = 220 grit and (e) Al ₂ O ₃ , d = 90-125 μ m	124
4-29	Scanning electron microphotographs of high-Cr white cast iron impacted surfaces at $\theta = 90^{\circ}$ by coarse particles of (a) SiO ₂ and (b) SiC. "Magnified views of central areas selected from Fig. (4-28)"	128
4-30	Scanning electron microphotographs of high-Cr white cast iron impacted surfaces at $\theta = 90^{\circ}$ by (a) coarse SiO ₂ and (b) fine SiO ₂ particles	129
4-31	Scanning electron microphotographs of high-Cr white cast iron impacted surfaces at $\theta = 90^{\circ}$ by fine particles of (a) SiO ₂ , (b) SiC and (c) Al ₂ O ₃	131
4-32	Scanning electron microphotographs of high-Cr white cast iron impacted surfaces at $\theta = 90^{\circ}$ by coarse particles of: (a) SiO ₂ and (b) SiC	133
4-33	Scanning electron microphotographs of high-Cr white cast iron impacted surfaces at $\theta = 90^{\circ}$ by coarse particles of: (a) SiO ₂ and (b) SiC	135
5-1	Relationship between erosion rate of 1017 steel and impact velocity at impingement angles of 30° and 90°	137
5-2	Relationship between erosion rate of high-Cr white cast iron and impact velocity at impingement angles of 30° and 90°	137
5-3	Relationship between weight loss of 1017 steel and particle concentration at impingement angles of 30° and 90°	139

5-4	Relationship between weight loss of high-Cr white cast iron and particle concentration at impingement angles of 30° and 90°	139
5-5	Relationship between erosion rate of 1017 steel and particle concentration at impingement angles of 30° and 90°	140
5-6	Relationship between erosion rate of high-Cr white cast iron and particle concentration at impingement angles of 30° and 90°	140
5-7	Scanning electron microphotographs of 1017 steel impacted surfaces at velocities of: (a) 5 m/s, (b) 10 m/s and (c) 15 m/s and at impingement angle of 30°	142
5-8	Scanning electron microphotographs of 1017 steel impacted surfaces at velocities of: (a) 5 m/s, (b) 10 m/s and (c) 15 m/s and at impingement angle of 30°. "Magnified views of selected areas from Fig. (5-7)"	143
5-9	Scanning electron microphotographs of 1017 steel impacted surfaces at velocities of: (a) 5 m/s, (b) 10 m/s and (c) 15 m/s and at impingement angle of 30°.	146
5-10	Typical microphotographs of 1017 steel impacted surfaces at velocity of 15 m/s and at impingement angle of 90°	148
5-11	Scanning electron microphotographs of 1017 steel impacted surfaces at particle concentration of: (a) 1 wt. % and (b) 3 wt. % and at impingement angle of 30°	150
5-12	Scanning electron microphotographs of 1017 steel impacted surfaces at particle concentration of: (a) 1 wt. % and (b) 3 wt. % and at impingement angle of 30°. "Magnified views of selected areas from Fig. (5-11)	151
5-13	Scanning electron microphotographs of 1017 steel impacted surfaces at particle concentration of: (a) 1 wt. % and (b) 3 wt. % and at impingement angle and impact velocity of 30° and 15 m/s, respectively.	152
5-14	Scanning electron microphotographs of high-Cr white cast iron impacted surfaces at velocities of: (a) 5 m/s, (b) 10 m/s and (c) 15 m/s and at impingement angle of 90°	154

5-15	Scanning electron microphotographs of high-Cr white cast iron impacted surfaces at velocities of: (a, b) 5 m/s, (c) 10 m/s and (d, e) 15 m/s and at impingement angle of 90°	156
5-16	Scanning electron microphotographs of high-Cr white cast iron impacted surfaces at particle concentration of: (a) 1 wt. % and (b) 3 wt. % and at impingement angle of 90°	160
5-17	Scanning electron microphotographs of high-Cr white cast iron impacted surfaces at particle concentration of: (a) 1 wt. % and (b) 3 wt. % and at impingement angle of 90°. "Magnified views of selected areas from Fig. (5-16)	161
5-18	Scanning electron microphotographs of high-Cr white cast iron impacted surfaces at particle concentration of: (a) 1 wt. % and (b) 3 wt. % and at impingement angle of 90°.	162

Nomenclature

A	μm^2	The projected area of the erodent particle
C	wt. %	The solid particle concentration
d	μm	The mean particle size
d_{ave}	μm	The measured average diameter of the particle
d_{max}	μm	The measured maximum diameter of the particle
d_{min}	μm	The measured minimum diameter of the particle
D	μm	The diameter of rotation of the rotor
E_m	(mg/kg)	Erosion rate
E_r	$(mg/mm^2/s)$	Another expression of the erosion rate
g	m/s^2	The gravitational acceleration
H_P	kgf/mm²	Hardness of the erodent particle
H_T	kgf/mm ²	Hardness of the target material
k		Constant
K		Constant
k_c	$MPa(m)^{0.5}$	Fracture toughness of the target material
I	mm	The total actual length of the test specimen
l_o	mm	The length of the specimen which is not exposed to the falling
		slurry stream
l_I	mm	The length of the specimen which is exposed to the falling slurry
		stream
L	mm	The length of the erodent particle
m		The particle size exponent
n		The impact velocity exponent
N	Hz	The rotational speed of the rotor

μm	The perimeter of the projected area of the erodent particle
ml/min.	The flow rate of the slurry stream
mm	The distance between the orifice and the specimen surface
min.	The erosion test time
m/s	The resultant impact velocity
m/s	The velocity of the falling slurry stream at the exiting orifice
m/s	The vertical velocity of the falling slurry stream at the specimen
	surface
m/s	The horizontal linear velocity
	The relative hardness exponent
mm	The width of the erodent particle
mm	The projected horizontal length of the specimen
mm	The projected vertical length of the specimen
	Constant
mg	The mass loss
degree	The impingement angle
degree	The mounting angle
degree	The rake angle
	ml/min. mm min. m/s m/s m/s m/s mm mm mm mm degree degree



STUDY OF THE BEHAVIOUR AND MECHANISM OF SLURRY العنوان:

> البخيتي، محمد احمد حمود على المؤلف الرئيسي:

احمد، شيمي محمد، عمارة، كرم محمد موسى، بدران، فاروق محمد مؤلفين آخرين:

فرید(مشرف)

2005 التاريخ الميلادي:

اسيوط موقع:

1 - 212 الصفحات:

586715 رقم MD:

رسائل جامعية نوع المحتوى:

> **English** اللغة:

رسالة دكتوراه الدرجة العلمية:

جامعة اسيوط الحامعة:

الكلىة: كلية الهندسة

> الدولة: مصر

قواعد المعلومات: Dissertations

الهندسة الميكانيكية، التآكل، السوائل، المواد الصلبة مواضيع:

https://search.mandumah.com/Record/586715 رابط:

© 2020 دار المنظومة. جميع الحقوق محفوظة.

ى كتاب استسونت بسيم الصور للصورية. هذه المادة متاحة بناء على الإتفاق الموقع مع أصحاب حقوق النشر، علما أن جميع حقوق النشر محفوظة. يمكنك تحميل أو طباعة هذه المادة للاستخدام الشخصي فقط، ويمنع النسخ أو التحويل أو النشر عبر أي وسيلة (مثل مواقع الانترنت أو البريد الالكتروني) دون تصريح خطي من أصحاب حقوق النشر أو دار المنظومة.



STUDY OF THE BEHAVIOUR AND MECHANISM OF **SLURRY EROSION**

BY

Mohamed Ahmed Hamoud Ali Al-Bukhaiti

M. Sc., Mechanical Engineering, Faculty of Engineering, Assiut University, Egypt, 2001

A THESIS

Submitted in partial fulfillment of the requirements for the degree of

DOCTOR OF PHILOSOPHY

In Mechanical Engineering

Department of Mechanical Engineering Faculty of Engineering, Assiut University Assiut, Egypt 2005

Supervised by:

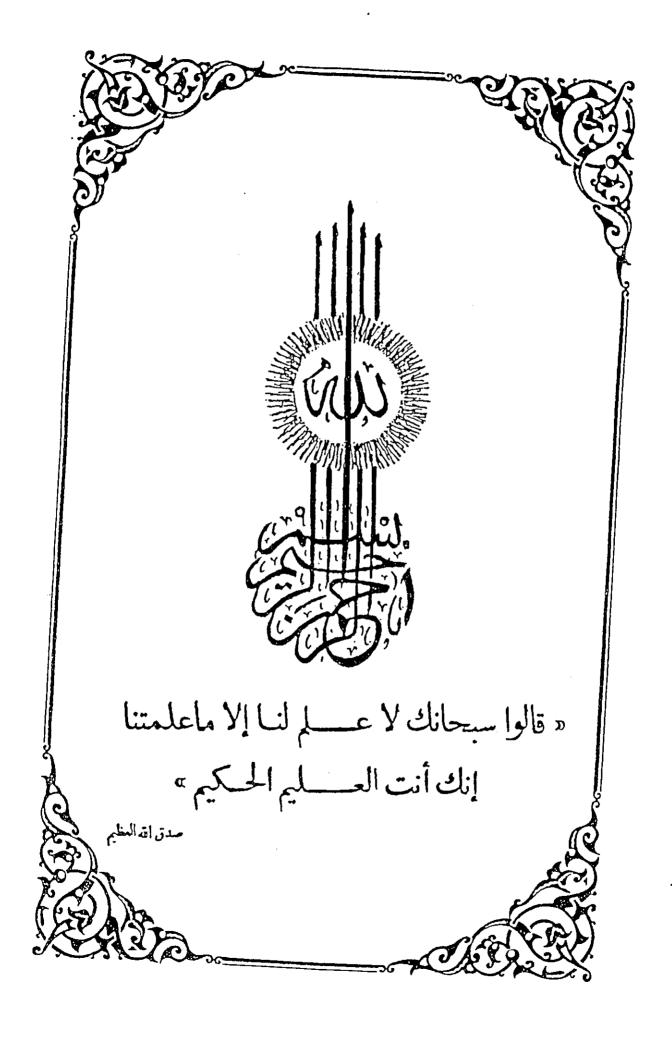
Prof. Dr. F. M. Badran

Prof. Dr. K. M. M. Emara

Dr. Shemy M. Ahmed

Prof. K.M.M. Emara Dmar

Dr. Shemy M. A.



My Parents

My Wife

My Children:

Nada, Islam and Karam)

Acknowledgments

First of all my gratitude and thanks to Allah, The Most Gracious and The Most Merciful.

I would like to express my heartfelt gratitude and deep appreciation to Prof. Dr. Farouk M. F. Badran, Prof. Dr. Karam M. M. Emara and Dr. Shemy M. Ahmed for their kind supervision, discussions, invaluable suggestions and guidance through the stages of research work which helped me to go along with the research work and preparing this thesis.

I would like also to express my gratitude and thanks to the staff members of the Department of Mechanical Engineering, Faculty of Engineering, Assiut University for their available cooperation.

I wish also to express my sincere thanks to Prof. Dr. Ahmed A. Abdel-Hamid, for the valuable information and discussions on determining the microstructure of the used materials.

Also my gratitude and thanks to the staff of workshop of the Department of Mechanical Engineering, Faculty of Engineering, Assiut University for their cooperation.

I wish also to thank Sana'a University, Republic of Yemen for providing the scholarship.

"All thanks are for every one helped me throughout the work in this thesis".

Mohamed A. HAL-Bukhaili

Abstract

In the present work a series of systematic slurry erosion tests were carried out to investigate the effect of different parameters on slurry erosion mechanisms and behaviour for ductile and brittle materials. These parameters include impingement angle, impact velocity, particle concentration, erodent particle characteristics, namely size, shape and hardness as well as target material hardness and microstructure. An apparatus for carrying out slurry erosion experiments was designed and manufactured. A series of accelerated erosion tests using a paint erosion indication technique has been carried out to calibrate and examine the reproducibility, capability and performance of the designed test rig.

The slurry erosion tests were carried out using the designed test rig on two different machinery materials, namely AISI 1017 steel and high-chromium white cast iron; and using three different types of erodent particles, namely silica sand, silicon carbide and alumina. The scanning electron microscopy, computer aided-image analysis technique, optical microscopy and gravimetric and microhardness measurements were utilized to identify the slurry erosion process.

Observations and analysis of the scanning electron microphotographs of specimen surfaces impacted for a short time at different slurry erosion conditions revealed that for 1017 steel the slurry erosion mechanisms are: ploughing, microcutting, indentation with extruded lips and fatigue wear. While, for high-Cr white cast iron the slurry erosion mechanisms are: cracking and gross fracture of the carbide phases as well as ploughing, microcutting and indentation with extruded lips for the ductile matrix. It was found that, in each particular case (test conditions) one or more of these mechanisms play the main role in the metal removal process, while others have a minor effect or not at all. Determination of the erosion mechanisms

helped greatly in the interpretation of the effect of the different parameters on the erosion rate in steady-state tests.

Test results showed that, the effect of impingement angle on erosion mechanisms of 1017 steel has three regions. These regions are: region of small impingement angles less than 20°, region of intermediate impingement angles between 20° and 70° and finally region of high impingement angles greater than 70°. These three regions are related to the tangential and normal components of the impacting force. The first region was characterized by shallow long scratches and limited chip formations resulting in small erosion rate. In the second region the formed wear tracks have deep and wide size and large chips were formed in front of the wear tracks, which explain the high erosion rate at intermediate impingement angles (maximum occurred at 45°). The third region was distinguished with relatively deep and elongated indentations with extruded material and small erosion rate. Consequently, it can be said that shallow ploughing and particle rolling were the dominant erosion mechanisms in the first region, microcutting and deep ploughing in the second region while indentations and material extrusion prevailed in the third region. For high-Cr white cast iron the test results showed that, the erosion mechanisms involved both plastic deformation of the ductile matrix and brittle fracture of the carbides. At low impingement angles (up to 45°) observations of microphotographs of the impacted surfaces revealed that, plastic deformation of the ductile matrix was the dominant erosion mechanism and the carbides fracture was negligible which lead to small erosion rate. Whereas, at high impingement angles (greater than 45°) gross fracture and cracking of the carbides in addition to indentation with extruded lips of the ductile matrix were the main erosion mechanisms.

The erodent particles, namely silica sand, silicon carbide and alumina were characterized in terms of their area (A), average diameter (d_{ave}), perimeter (P), length (L) and width (W). The aspect ratio (W/L) and the roundness factor ($P^2/4\pi A$) were used as the indicators of particle shape. It was found that the regularity and circularity

in shape of silica sand and alumina particles increased with the increase of particle sizes, while decreased for silicon carbide particles. Test results revealed that, with fine erodent particles plastic indentation accompanied by extruded material was the dominant erosion mechanism for 1017 steel and high-Cr white cast iron irrespective of the impingement angle and erodent type or shape. For 1017 steel and at impingement angle of 30°, results showed that ploughing and microcutting were the main erosion mechanisms when the target surface is impacted by coarse SiC and SiO₂ particles. The role of microcutting in the metal removal process increased with the increase of particle angularity and sharpness as in the case of silicon carbide particles. As well as the angularity and sharpness of silicon carbide particles yielded serrated tracks rather than smooth tracks obtained with regular and rounded silica sand particles for the same size. It was also shown that the lips and chips formed due to indentation and ploughing mechanisms were finally detached from the target surface by fatigue. It was also observed that microcracks initiated at many locations on the eroded area such as, chips and lips which were subjected to severe plastic deformation, serrations of ploughing tracks and traces of polishing lines. For high-Cr white cast iron and at normal incidence, test results showed that with impacting by coarse particles, fracture and cracking of the carbides in addition to plastic indentation with lips of the ductile matrix were the main erosion mechanisms depending on the particle shape. The angularity and sharpness of silicon carbide particles yielded severe erosion damage included gross fracture associated with formation of many lateral cracks of the carbides rather than mild erosion damage obtained with regular and rounded silica sand particles for a comparable size. The results also showed that the hardness of erodent particles has a pronounced effect on the material removal mechanism.

Test results showed that the role of the impact velocity in developing erosion damage is related to the variation of the erosion mechanisms which depend upon the kinetic energy of the impacting particles. At low impact velocity (5 m/s) and at impingement angle of 30°, microscopic observations of damaged surfaces of 1017 steel revealed that, indentation with extruded lips was the dominant erosion

mechanism. Whereas, at high impact velocity ploughing was the main erosion mechanism. The length of the wear tracks developed by ploughing mechanism depends upon the impact velocity. For high-Cr white cast iron and at normal incidence, test results showed that the erosion mechanism of indentation with extruded lips of the ductile matrix prevailed at low impact velocity (5 m/s). Whereas, at intermediate impact velocity (10 m/s) plastic indentation of the ductile matrix in addition to some fracture of the carbides were the dominant erosion mechanisms. For high impact velocity (15 m/s) fracture and cracking of the carbides besides to indentation of the ductile matrix were the dominant erosion mechanisms.

Test results showed that the weight loss from the surface of the test specimens increases with the increase of solid particle concentration. But the erosion rate (expressed in terms of mass loss per mass of erodent particles) increases at low particle concentration up to 1 wt.%. Then it decreases rapidly attaining nearly steady state behaviour. Observations of scanning electron microphotographs revealed that the erosion mechanisms at particle concentration of 1 wt.% and 3 wt.% are the same. It was also observed that the intensity of erosion damage at particle concentration of 3 wt.% is higher than that for particle concentration of 1 wt.%. This was attributed to repeated multiple impacts which occur at higher particle concentration resulting in large sizes of wear scar.

Table of Contents

Cŀ	Chapter	
I.	Introduction and Literature Review	1
	1-1 Introduction	1
	1-2 Literature Review	4
	1-3 Impingement Angle	4
	1-4 Particle Velocity	7
	1-5 Particle Concentration	10
	1-6 Particle Characterization	13
	1-6-1 Particle size	13
	1-6-2 Particle shape	14
	1-6-3 Particle hardness	17
	1-6-4 Particle degradation	18
	1-7 Target Material Properties	19
	1-8 Test Methods	21
	1-8-1 Pipelines	21
	1-8-2 Laboratory test rigs	22
	 i Jet impingement tester ii A centrifugal erosion test fixture iii Flow-through slurry wear test equipment iv Slurry pot testers 	22 22 22 24
	1-9 Scope of the Present Work	27
]	I. Experimental Work	28
	2-1 Introduction	28
	2-2 Slurry Erosion Test Rig	. 29
	2-2-1 Calibration	. 55
	2-2-2 Determination of test parameters	. 35

velocity	. 35 . 37
2and Capability of the Designed Apparatus	
Per mance of the tester with four rotating arms	. 37
2-3 Per aducibility of the tester	. 38
oducibility of the tester	40
fiability of the tester	42
1- Effect of exposure time 2- Effect of impingement angle 3- Effect of impact velocity 4- Effect of particle concentration	. 42 45 45 48
arget Materials	50
2-4-1 AISI 1017 Steel	50
2-4-2 High-chromium white cast iron	
2-5 Erodent Particles	52
2-6 Measuring Devices	57
	58
1- Topographic features of eroded surfaces	58 58
3- Erodent particle characterization	58
4- Surface roughness measurement	58
5- Microhardness measurement	59
2-7 Experimental Procedure	59
III. Effect of Impingement Angle on Slurry Erosion Behaviour and	
Mechanisms	61
3-1 Introduction	61
3-2 Effect of Impingement Angle on Erosion Beahviour and Mechanisms of 1017 Steel	61
3-2-1 Erosion rate	61
3-2-2 Configuration of eroded surfaces	62
3-2-3 Microscopy observations of impacted surfaces	64 73
3-3 Effect of Impingement Angle on Erosion Behaviour and Mechanisms of High-Cr White Cast Iron	78
3-3-1 Erosion rate	80
3-3-2 Microscopy observations and erosion mechanisms	80

3-4 Erosion Behaviour and Mechanisms of 1017 Steel and High-Cr White Cast Iron with Impingement Angles	87
IV. Effect of Particle Characteristics on Slurry Erosion Behaviour and Mechanisms	91
4-1 Erodent Particle Characterization	91
4-2 Effect of Particle Characteristics on Erosion Rate	101
4-2-1 Effect of particle size	101 105 106
4-3 Microscopy Observations and Erosion Mechanisms of 1017 Steel	108
4-3-1 Effect of particle size	108 112 114 114
4-4 Microscopy Observations and Erosion Mechanisms of High-Cr White Cast Iron	121
4-4-1 Effect of particle size	121 130 134
V. Effect of Impact Velocity and Particle Concentration on Slurry Erosion Behaviour and Mechanisms	136
5-1 Effect of Impact Velocity on Erosion Rate	136
5-2 Effect of Particle Concentration on Erosion Rate	138
5-3 Microscopy Observations and Erosion Mechanisms of 1017 Steel	141
5-3-1 Effect of impact velocity	141 149
5-4 Microscopy Observations and Erosion Mechanisms of High-Cr White Cast Iron	149
5-4-1 Effect of impact velocity	149 159
VI. Conclusions	164

Refere	ences	168
	ndices	
A. Analysis of the rotating arms dynamics of the designed apparatus	179	
В.	Solidification sequences and microstructure of high-Cr white cast iron	
	alloy	184

List of Tables

Table		page
1-1	Parameters influencing slurry erosion	2
1-2	Experimental values of the velocity exponent n for slurry erosion reported in the literature	9
2-1	Results of reproducibility tests	42
2-2	Chemical composition of 1017 steel	52
2-3	Mechanical properties of 1017 steel	52
2-4	Chemical composition of high-Cr white cast iron alloy	55
2-5	Bulk hardness and microhardness of high-Cr white cast iron alloy	55
2-6	Size ranges and suppliers of particles	57
2-7	Values of the studied slurry erosion parameters and test conditions	60
4-1	Statistical values of particle parameters (size and shape) as obtained by image analysis processing of SiO ₂ particles	97
4-2	Statistical values of particle parameters (size and shape) as obtained by image analysis processing of SiC particles	97
4-3	Statistical values of particle parameters (size and shape) as obtained by image analysis processing of Al ₂ O ₃ particles	98
A-1	Calculated values of the specimen surface length which is exposed to the slurry stream at: $v = 10$ m/s, $v_2 = 9.89$ m/s, $N = 12.7$ Hz and $\theta' = 9.2^{\circ}$, using four rotating arms	182
A-2	Calculated values of the specimen surface length which is exposed to the slurry stream at: $v = 15$ m/s, $v_2 = 14.96$ m/s, $N = 19.2$ Hz and $\theta' = 6.3^{\circ}$, using four rotating arms	182

A-3	Calculated values of the specimen surface length which is exposed to the slurry stream at: $v = 15$ m/s, $v_2 = 14.96$ m/s, $N = 19.2$ Hz and $\theta' = 6.3^{\circ}$, using two rotating arms	182
A-4	Calculated values of the specimen surface length which is exposed to the slurry stream at: $v = 20$ m/s, $v_2 = 19.95$ m/s, $N = 25.6$ Hz and $\theta' = 4.6^{\circ}$, using two rotating arms	183

List of Figures

Figure		page
1-1a	Erosion of needle in needle and seat choke [12]	3
1-1b	A Pelton turbine runner destroyed by advanced wall erosion [13]	3
1-1c	Surface erosion of the inside of a Francis turbine [13]	3
1-1d	Eroded stainless steel needle of a 2-nozzle Pelton turbine [13]	3
1-1e	Pump impeller failure due to erosion [14]	3
1-2	Erosion rate as a function of impact angle for Aluminum, Copper, Mild steel and Alumina eroded by silica sand (600-1000 μ m), slurry at $\nu = 5.3$ m/s and C = 17 wt. % [20]	6
1-3	 (a) Dependence of erosion rate for Al₂O₃ on impact angle. (b) Dependence of erosion rate for zirconia, silaon and SiC on impact angle [21] 	6
1-4	Erosion vs. slurry velocity for hot-rolled 1018 steel in 30 wt.% coal-kerosene slurry at 95°C at various impingement angles [40]	8
1-5	Velocity-wear relationship: •, Aluminum; O, Cast iron; +, Ceramic Steel [41]	8
1-6	Relationship between wear rate and jet velocity [6]	8
1-7	Effect of velocity on the erosion rate of iron for a range of erodent sizes: (a) alumina and (b) silicon carbide [42]	11
1-8	Relationship between wear rate and silica sand concentration [6]	12
1-9	Variation of erosion rate as a function of cumulative weight of the erodent under oblique impact angle for Ni in A2-treated condition [47]	12
1-10	Relationship between wear rate and particle size [6]	15

1-11	Definition of particle size by means of three mutually perpendicular dimensions [60]	15
1-12	Schematic diagram of the pilot plant [93]	23
1-13	Schematic diagram of slurry jet erosion rig [41]	23
1-14	Schematic diagram of a centrifugal slurry erosion test fixture [95]	25
1-15	Schematic diagram of flow-through slurry wear test apparatus [95]	25
1-16	Schematic diagram of the slurry erosion pot tester [50]	26
2-1	Schematic diagram of the designed slurry erosion apparatus	30
2-2a	Photograph of the slurry erosion test rig, "General view"	31
2-2b,c	Photograph of the designed slurry erosion test rig: (b) Vacuum test chamber and (c) Rotating test specimens exposed to falling slurry stream	32
2-3	Schematic diagram of the specimen holder and the impingement angle indicator	34
2-4	Calibration curve for the speed controller unit	34
2-5	Measured rate of slurry flow and solid particle concentration in slurry: (a) $C = 2$ wt. % and (b) $C = 10$ wt. %, erodent (250-355 $\mu m SiO_2$)	36
2-6	Schematic diagram of impact velocity and impingement angle	39
2-7	Photographs of the eroded paint surfaces using four rotating arms at different test durations and test conditions: $v = 15$ m/s, $C = 1$ wt. % and $d = 302$ μ m; (a) $\theta = 30^{\circ}$, (b) $\theta = 45^{\circ}$, (c) $\theta = 60^{\circ}$ and (d) $\theta = 90^{\circ}$	39
2-8	Schematic diagram of (a) four rotating arms, (b) resultant angle of impact and (c) dynamic location of specimens with respect to the falling slurry stream	41

2-9	Photographs of the eroded paint surfaces using two rotating arms at test conditions: $v = 15$ m/s, $C = 1$ wt. %, $d = 302$ μ m and $t = 4$ min	41
2-10	Photographs of the eroded paint surfaces at different test durations and test conditions as: $v = 15$ m/s, $d = 302$ μ m, and $C = 1$ wt.%	44
2-11	Erosion rate of paint material as a function of test duration for different impingement angles at: $v = 15$ m/s, $d = 302$ µm and $C = 1$ wt. %	44
2-12	Photographs of the eroded paint surfaces at different impingement angles and test conditions as: $v = 15$ m/s, $d = 302$ μ m, $C = 1$ wt.% and $t = 4$ min.	46
2-13	Relationship between erosion rate of paint material and impingement angle at: $v = 15$ m/s, $d = 302$ μ m, $C = 1$ wt. %, and $t = 4$ min	46
2-14	Photographs of the eroded paint surfaces at different impact velocities and test conditions as: $d = 302 \mu m$, $C = 1 \text{ wt.}\%$ and $t = 4 \text{ min.}$	47
2-15	Relationship between erosion rate of paint material and impact velocity for different impingement angles at: $d = 302 \mu m$, $C = 1 wt$. %, and $t = 4 min$.	47
2-16	Variation of weight loss of the paint material versus particle concentration at different impingement angles and at: $v = 15$ m/s, $d = 302 \mu m$ and $t = 2$ min.	49
2-17	Relationship between weight loss of paint material and particle concentration for different impingement angles at: $v = 15$ m/s, $d = 302$ μm and $t = 2$ min.	49
2-18	Dimensions of (a) Slurry erosion test specimen and (b) Holder of the test specimen	51
2-19	Optical (a) and SEM (b) photographs of 1017 steel microstructure	54
2 - 20a,b	Optical photographs of High-Cr white cast iron microstructure	54
2-21a,b	SEM photographs of high-Cr white cast iron microstructure	54
2-22	Fe-Cr-C ternary phase diagram: (a) liquidus surface projection of the system and (b) isothermal section at 700°C	56

3-1	Cumulative Mass loss of 1017 steel as a function of test duration for different impingement angles	63
3-2	Relationship between erosion rate of 1017 steel and impingement angle for different test durations	63
3-3	Photographs of 1017 steel eroded surfaces at different values of impingement angles and at test time of (a) 10 min. and (b) 60 min	65
3-4	Relationship between the micro-hardness of 1017 steel eroded surfaces and impingement angle after test time of 60 min.	65
3-5	Scanning electron microphotographs of 1017 steel impacted surfaces at various impingement angles: (a) 15°, (b) 30°, (c) 45°, (d) 60° and (e) 90°	67
3-6	Scanning electron microphotographs of 1017 steel impacted surfaces at various impingement angles: (a) 15°, (b) 30°, (c) 45°, (d) 60° and (e) 90°. "Magnified views of selected areas from Fig. (3-5)"	70
3-7	Scanning electron microphotographs of 1017 steel impacted surfaces at various impingement angles: (a) 15°, (b) 30°, (c) 45°, (d) 60°, (e) 75° and (f) 90°.	74
3-8	Scanning electron microphotographs of 1017 steel impacted surfaces at high impingement angles: (a) 75° and (b) 90°. "Indented pits and extruded lips	79
3-9	Cumulative Mass loss of high-Cr white cast iron as a function of test duration for different impingement angles	81
3-10	Relationship between erosion rate of high-Cr white cast iron and impingement angle for different test durations	81
3-11	Scanning electron microphotographs of high-Cr white cast iron impacted surfaces at different impingement angles: (a) 30°, (b) 45°, (c) 60° and (d) 90°	82
3-12	Scanning electron microphotographs of high-Cr white cast iron impacted surfaces at different impingement angles: (a) 30°, (b) 45°, (c) 60° and (d) 90°.	85

3-13	function of erosion rate and erosion mechanisms of 1017 steel as a function of impingement angle at impact velocity of 15 m/s	89
3-14	Variation of erosion rate and erosion mechanisms of high-Cr white cast iron as a function of impingement angle at impact velocity of 15 m/s	90
4-1	Scanning electron microphotographs of silica sand particles	93
4-2	Scanning electron microphotographs of silicon carbide particles	94
4-3	Scanning electron microphotographs of alumina particles	96
4-4	Relationship between the aspect ratio and the measured average size for SiO ₂ , SiC and Al ₂ O ₃ particles	99
4-5	Relationship between the roundness factor (perimeter) ² / 4π Area and the measured average size for SiO ₂ , SiC and Al ₂ O ₃ particles	99
4-6	Percent cumulative frequency distribution curve of aspect ratios of SiO ₂ particles	100
4-7	Percent cumulative frequency distribution curve of aspect ratios of SiC particles	100
4-8	Percent cumulative frequency distribution curve of aspect ratios of Al ₂ O ₃ particles	100
4-9	Percent cumulative frequency distribution curve of $(perimeter)^2/4\pi Area$ ratios of SiO ₂ particles	102
4-10	Percent cumulative frequency distribution curve of (perimeter) $^2/4\pi$ Area ratios of SiC particles	102
4-11	Percent cumulative frequency distribution curve of (perimeter) $^2/4\pi$ Area ratios of Al ₂ O ₃ particles	102
4-12	Variation of erosion rate of 1017 steel as a function of particle sizes for different erodents, $\theta = 30^{\circ}$	103
4-13	Variation of erosion rate of high-Cr white cast iron as a function of particle sizes for different erodents, $\theta = 30^{\circ}$	103

4-14	Variation of erosion rate of 1017 steel as a function of particle sizes for different erodents, $\theta = 90^{\circ}$	104
4-15	Variation of erosion rate of high-Cr white cast iron as a function of particle sizes for different erodents, $\theta = 90^{\circ}$	104
4-16	Relationship between the erosion rate of 1017 steel and the relative hardness of the erodent particles and target material at $v = 15$ m/s, $d = (125-180 \mu m)$, $\theta = 30^{\circ}$ and $C = 1$ wt. %	107
4-17	Relationship between the erosion rate of high-Cr white cast iron and the relative hardness of the erodent particles and target material at $v=15$ m/s, $d=(125-180 \mu m)$, $\theta=30^{\circ}$ and $C=1$ wt. %	107
4-18	Scanning electron microphotographs of 1017 steel impacted surfaces at $\theta=30^{\circ}$ by different particles having different sizes: (a) SiO ₂ , $d=500-710$ µm; (b) SiO ₂ , $d=90-125$ µm; (c) SiC, $d=24$ grit; (d) SiC, $d=220$ grit and (e) Al ₂ O ₃ , $d=90-125$ µm.	109
4-19	Calculated trajectories of sand particles of different diameters in a water jet 20 mm wide and velocity 8 m/s directed at flat plate [121]	111
4-20	Scanning electron microphotographs of 1017 steel impacted surfaces at $\theta = 30^{\circ}$ by coarse particles of (a) SiO ₂ and (b) SiC. "Magnified views of central areas selected from Fig. (4-18)"	113
4-21	Scanning electron microphotographs illustrating typical examples of (a) rounded SiO ₂ and (b) angular SiC particles	115
4-22	Scanning electron microphotographs of 1017 steel impacted surfaces at $\theta = 30^{\circ}$ by coarse particles of (a) SiO ₂ and (b) SiC. "Letter R denotes formation of microcrack on some traces of polishing lines	116
4-23	Scanning electron microphotographs of 1017 steel impacted surfaces at $\theta = 30^{\circ}$ by coarse SiC particles. The letter C indicates the formation of microcrack on the impacted surface	118
4-24	Scanning electron microphotographs of 1017 steel impacted surfaces at $\theta = 30^{\circ}$ by fine particles of (a) SiO ₂ , (b) SiC and (c) Al ₂ O ₃	118

4-25	Scanning electron microphotographs of 1017 steel impacted surfaces at $\theta = 30^{\circ}$ by fine particles of (a) SiO ₂ and (b) SiC. Directionality is clear in the surface features	120
4-26	Schematic for particle impacting on a target surface: (a) angular particle with positive rake angle, α , (b) rounded particle with negative rake angle and (c) angular particle with negative rake angle	122
4-27	Scanning electron microphotographs of 1017 steel impacted surfaces at $\theta = 30^{\circ}$ by coarse particles of (a) SiO ₂ and (b) SiC	122
4-28	Scanning electron microphotographs of high-Cr white cast iron impacted surfaces at $\theta = 90^{\circ}$ by different particles having different sizes: (a) SiO ₂ , d = 500-710 μ m; (b) SiO ₂ , d = 90-125 μ m; (c) SiC, d = 24grit; (d) SiC, d = 220 grit and (e) Al ₂ O ₃ , d = 90-125 μ m	124
4-29	Scanning electron microphotographs of high-Cr white cast iron impacted surfaces at $\theta = 90^{\circ}$ by coarse particles of (a) SiO ₂ and (b) SiC. "Magnified views of central areas selected from Fig. (4-28)"	128
4-30	Scanning electron microphotographs of high-Cr white cast iron impacted surfaces at $\theta = 90^{\circ}$ by (a) coarse SiO ₂ and (b) fine SiO ₂ particles	129
4-31	Scanning electron microphotographs of high-Cr white cast iron impacted surfaces at $\theta = 90^{\circ}$ by fine particles of (a) SiO ₂ , (b) SiC and (c) Al ₂ O ₃	131
4-32	Scanning electron microphotographs of high-Cr white cast iron impacted surfaces at $\theta = 90^{\circ}$ by coarse particles of: (a) SiO ₂ and (b) SiC	133
4-33	Scanning electron microphotographs of high-Cr white cast iron impacted surfaces at $\theta = 90^{\circ}$ by coarse particles of: (a) SiO ₂ and (b) SiC	135
5-1	Relationship between erosion rate of 1017 steel and impact velocity at impingement angles of 30° and 90°	137
5-2	Relationship between erosion rate of high-Cr white cast iron and impact velocity at impingement angles of 30° and 90°	137
5-3	Relationship between weight loss of 1017 steel and particle concentration at impingement angles of 30° and 90°	139

5-4	Relationship between weight loss of high-Cr white cast iron and particle concentration at impingement angles of 30° and 90°	139			
5-5	Relationship between erosion rate of 1017 steel and particle concentration at impingement angles of 30° and 90°				
5-6	Relationship between erosion rate of high-Cr white cast iron and particle concentration at impingement angles of 30° and 90°	140			
5-7	Scanning electron microphotographs of 1017 steel impacted surfaces at velocities of: (a) 5 m/s, (b) 10 m/s and (c) 15 m/s and at impingement angle of 30°				
5-8	Scanning electron microphotographs of 1017 steel impacted surfaces at velocities of: (a) 5 m/s, (b) 10 m/s and (c) 15 m/s and at impingement angle of 30°. "Magnified views of selected areas from Fig. (5-7)"				
5-9	Scanning electron microphotographs of 1017 steel impacted surfaces at velocities of: (a) 5 m/s, (b) 10 m/s and (c) 15 m/s and at impingement angle of 30°.				
5-10	Typical microphotographs of 1017 steel impacted surfaces at velocity of 15 m/s and at impingement angle of 90°				
5-11	Scanning electron microphotographs of 1017 steel impacted surfaces at particle concentration of: (a) 1 wt. % and (b) 3 wt. % and at impingement angle of 30°				
5-12	Scanning electron microphotographs of 1017 steel impacted surfaces at particle concentration of: (a) 1 wt. % and (b) 3 wt. % and at impingement angle of 30°. "Magnified views of selected areas from Fig. (5-11)				
5-13	Scanning electron microphotographs of 1017 steel impacted surfaces at particle concentration of: (a) 1 wt. % and (b) 3 wt. % and at impingement angle and impact velocity of 30° and 15 m/s, respectively.	152			
5-14	Scanning electron microphotographs of high-Cr white cast iron impacted surfaces at velocities of: (a) 5 m/s, (b) 10 m/s and (c) 15 m/s and at impingement angle of 90°	154			

5-15	Scanning electron microphotographs of high-Cr white cast iron impacted surfaces at velocities of: (a, b) 5 m/s, (c) 10 m/s and (d, e) 15 m/s and at impingement angle of 90°	156
5-16	Scanning electron microphotographs of high-Cr white cast iron impacted surfaces at particle concentration of: (a) 1 wt. % and (b) 3 wt. % and at impingement angle of 90°	
5-17	Scanning electron microphotographs of high-Cr white cast iron impacted surfaces at particle concentration of: (a) 1 wt. % and (b) 3 wt. % and at impingement angle of 90°. "Magnified views of selected areas from Fig. (5-16)	161
5-18	Scanning electron microphotographs of high-Cr white cast iron impacted surfaces at particle concentration of: (a) 1 wt. % and (b) 3 wt. % and at impingement angle of 90°.	162

Nomenclature

A	μm^2	The projected area of the erodent particle
C	wt. %	The solid particle concentration
d	μm	The mean particle size
d_{ave}	μm	The measured average diameter of the particle
d_{max}	μm	The measured maximum diameter of the particle
d_{min}	μm	The measured minimum diameter of the particle
D	μm	The diameter of rotation of the rotor
E_m	(mg/kg)	Erosion rate
E_r	$(mg/mm^2/s)$	Another expression of the erosion rate
g	m/s^2	The gravitational acceleration
H_P	kgf/mm²	Hardness of the erodent particle
H_T	kgf/mm ²	Hardness of the target material
k		Constant
K		Constant
k_c	$MPa(m)^{0.5}$	Fracture toughness of the target material
I	mm	The total actual length of the test specimen
l_o	mm	The length of the specimen which is not exposed to the falling
		slurry stream
l_I	mm	The length of the specimen which is exposed to the falling slurry
		stream
L	mm	The length of the erodent particle
m		The particle size exponent
n		The impact velocity exponent
N	Hz	The rotational speed of the rotor



STUDY OF THE BEHAVIOUR AND MECHANISM OF SLURRY العنوان:

> البخيتي، محمد احمد حمود على المؤلف الرئيسي:

احمد، شيمي محمد، عمارة، كرم محمد موسى، بدران، فاروق محمد مؤلفين آخرين:

فرید(مشرف)

2005 التاريخ الميلادي:

اسيوط موقع:

1 - 212 الصفحات:

586715 رقم MD:

رسائل جامعية نوع المحتوى:

> **English** اللغة:

رسالة دكتوراه الدرجة العلمية:

جامعة اسيوط الحامعة:

الكلىة: كلية الهندسة

> الدولة: مصر

قواعد المعلومات: Dissertations

الهندسة الميكانيكية، التآكل، السوائل، المواد الصلبة مواضيع:

https://search.mandumah.com/Record/586715 رابط:

© 2020 دار المنظومة. جميع الحقوق محفوظة.

ى كتاب استسونت بسيم الصور للصورية. هذه المادة متاحة بناء على الإتفاق الموقع مع أصحاب حقوق النشر، علما أن جميع حقوق النشر محفوظة. يمكنك تحميل أو طباعة هذه المادة للاستخدام الشخصي فقط، ويمنع النسخ أو التحويل أو النشر عبر أي وسيلة (مثل مواقع الانترنت أو البريد الالكتروني) دون تصريح خطي من أصحاب حقوق النشر أو دار المنظومة.



STUDY OF THE BEHAVIOUR AND MECHANISM OF **SLURRY EROSION**

BY

Mohamed Ahmed Hamoud Ali Al-Bukhaiti

M. Sc., Mechanical Engineering, Faculty of Engineering, Assiut University, Egypt, 2001

A THESIS

Submitted in partial fulfillment of the requirements for the degree of

DOCTOR OF PHILOSOPHY

In Mechanical Engineering

Department of Mechanical Engineering Faculty of Engineering, Assiut University Assiut, Egypt 2005

Supervised by:

Prof. Dr. F. M. Badran

Prof. Dr. K. M. M. Emara

Dr. Shemy M. Ahmed

Prof. K.M.M. Emara Dmar

Dr. Shemy M. A.

دراسة سلوك وآلية التآكل الناتج عن سريان سائل به عوالق صلبة

رسالة مقدمة من:

المهندس / محمد أحمد حمود على البخيتي

المدرس المساعد بقسم الهندسة الميكانيكية - جامعة صنعاء- الجمهورية اليمنية بكالوريوس هندسة الإنتاج - الجامعة التكنولوجية - بغداد 1996 م ماجستير في الهندسة الميكانيكية- كلية الهندسة - جامعة أسيوط- 2001م

للحصول على درجة الدكترواة في الهندسة الميكانيكية

لجنة الحكم عل الرسالة:

أ.د. مختار عمر عباس مختار

أ.د. محمود غريب الشربيني

أ.د. فاروق محمد فريد بدران

أ.د. كرم محمد موسى عمارة

د. شيمي محميد أهيد

تحت إشـــراف:

أ.د. فاروق محمد فريد بدران

أ.د. كرم محمد موسى عمارة

د. شيمي محمد أحمد

مايو 2005 م